


Three-Dimensional Numerical Modeling of Surface-Acoustic-Wave Devices: Acoustophoresis of Micro- and Nanoparticles Including Streaming

Nils R. Skov^{1,*}, Prateek Sehgal^{2,†}, Brian J. Kirby^{2,3,‡} and Henrik Bruus^{1,§}

¹*Department of Physics, Technical University of Denmark, DTU Physics Building 309, DK-2800 Kongens Lyngby, Denmark*

²*Sibley School of Mechanical and Aerospace Engineering, Cornell University, Ithaca, New York 14853, USA*

³*Department of Medicine, Division of Hematology and Medical Oncology, Weill-Cornell Medicine, New York, New York 10021, USA*

 (Received 26 June 2019; revised manuscript received 12 September 2019; published 14 October 2019)

Surface-acoustic-wave (SAW) devices form an important class of acoustofluidic devices, in which acoustic waves are generated and propagate along the surface of a piezoelectric substrate. Despite their widespread use, only a few fully three-dimensional (3D) numerical simulations have been reported in the literature. In this paper, we present a 3D numerical simulation taking into account the electromechanical fields of the piezoelectric SAW device, the acoustic displacement field in the attached elastic material, in which a liquid-filled microchannel is embedded, the acoustic fields inside the microchannel, and the resulting acoustic radiation force and streaming-induced drag force acting on micro- and nanoparticles suspended in the microchannel. A specific device design is presented, for which numerical predictions of the acoustic resonances and the acoustophoretic response of suspended microparticles in three dimensions are successfully compared with experimental observations. The simulations provide a physical explanation of the observed qualitative difference between devices with acoustically soft and hard lids in terms of traveling and standing waves, respectively. The simulations also correctly predict the existence and position of the observed in-plane streaming-flow rolls. The simulation model presented may be useful in the development of SAW devices optimized for various acoustofluidic tasks.

DOI: [10.1103/PhysRevApplied.12.044028](https://doi.org/10.1103/PhysRevApplied.12.044028)

I. INTRODUCTION

During the past decade, surface-acoustic-wave (SAW) devices have been developed for a multitude of different types of acoustofluidic handling of micrometer-sized particles inside closed microchannels. Examples include acoustic mixing [1], continuous particle or droplet focusing [2,3] and separation [4,5], single-particle handling [6,7], acoustic tweezing [8–10], two-dimensional single-cell patterning [11,12], on-chip studies of microbial organisms [13,14], and nontrivial electrode shapes to generate chirped, focused, and rotating acoustic waves [10,15–17].

The development of the effective handling of submicrometer-sized particles has been less successful. It remains a challenge in biotechnology to handle this highly important class of particles that includes small bacteria, exosomes, and viruses. If these particles could be handled in a controlled way, it would be of particular interest for

developing new and more efficient diagnostics [18]. The first steps towards acoustofluidic handling of nanometer-sized particles were taken by relying on acoustic-streaming effects with both bulk acoustic waves (BAWs) [19] and SAWs [20], or by using seed particles to enhance acoustic trapping in BAW devices [21]. However, these streaming-based methods have low selectivity. More recently, SAW devices have been developed to focus [22] and separate [23,24] nanoparticles. In particular, Sehgal and Kirby [23] demonstrated separation between 100-nm- and 300-nm-diameter particles at a proof-of-concept stage. To fully utilize the potential of this and similar devices, further development is necessary to increase the efficiency and the sorting flow rates. Here, numerical simulations may play a crucial role, both in improving the understanding of the underlying physical acoustofluidic processes, and in easing the cumbersome development cycle consisting of an iterative series of creating, fabricating, and testing device designs.

An increasing amount of numerical studies include piezoelectric dynamics in two-dimensional (2D) models [25–28], but in most cases the piezoelectric transducers are introduced in numeric models in the form of

*nilsre@fysik.dtu.dk

†ps824@cornell.edu

‡kirby@cornell.edu

§bruus@fysik.dtu.dk

analytic approximations [29–34], and designs are often based on *a priori* knowledge of the piezoelectric effect in the unloaded substrates typically applied in telecommunications. In acoustofluidic devices, the acoustic impedance of the contacting fluid is much closer to that of the substrate, causing waves to behave very differently from those in telecommunications devices. It is thus prudent to include the piezoelectric effect and the coupling between the fluid and substrate in numeric models to accurately describe device behavior. Additionally, three-dimensional (3D) simulations in the literature are scarce and do not include both the actuators and acoustic streaming, and this is essential for making full-device acoustophoresis predictions as many actual acoustofluidic devices exhibit non-trivial features in three dimensions due to the asymmetric and intricate shapes of the electrodes and channels.

In this paper, we present 3D numerical simulations that improve on previous work by taking into account all, and not just some, of the following central aspects: the electromechanical fields of the piezoelectric SAW device, the acoustic displacement field in the attached elastic material in which the liquid-filled microchannel is embedded, the acoustic fields inside the microchannel, and the resulting acoustic radiation force and streaming-induced drag force acting on microparticles suspended in the microchannel. The model is validated experimentally with devices based on the SAW device described by Sehgal and Kirby [23]. In Sec. II we describe the physical model system representing the SAW device and state the governing equations, and in Sec. III we treat the implementation of the model system in a weak-form finite-element model. The results of the model in reduced 2D form and in the full 3D form are presented in Secs. V and VI, and, finally, in Secs. VII and VIII we discuss our findings, point out the predictive power of our model, and summarize our conclusions.

II. THE MODEL SAW SYSTEM AND THE GOVERNING EQUATIONS

The model SAW system is shown in Fig. 1(a). Essentially, it consists of a piezoelectric lithium niobate substrate with a specific interdigitated-transducer (IDT) metal-electrode configuration on the surface. On top of the substrate, a microfluidic channel is defined in an elastic material, either acoustically soft polydimethylsiloxane (PDMS) polymer rubber or acoustically hard borosilicate (Pyrex) glass.

We follow Sehgal and Kirby [23] and place the IDT electrodes directly underneath the microchannel and choose the periodicity of the electrode pattern to result in a SAW wavelength $\lambda_{\text{SAW}} = 80 \mu\text{m}$ and an (unloaded) resonance frequency $f_{\text{SAW}} = c_{\text{SAW}}/\lambda_{\text{SAW}} = (3995 \text{ m/s})/(80 \mu\text{m}) = 49.9 \text{ MHz}$. The driving electrodes are flanked by Bragg-reflector electrodes to (partially) reflect the outgoing SAWs traveling along the surface from

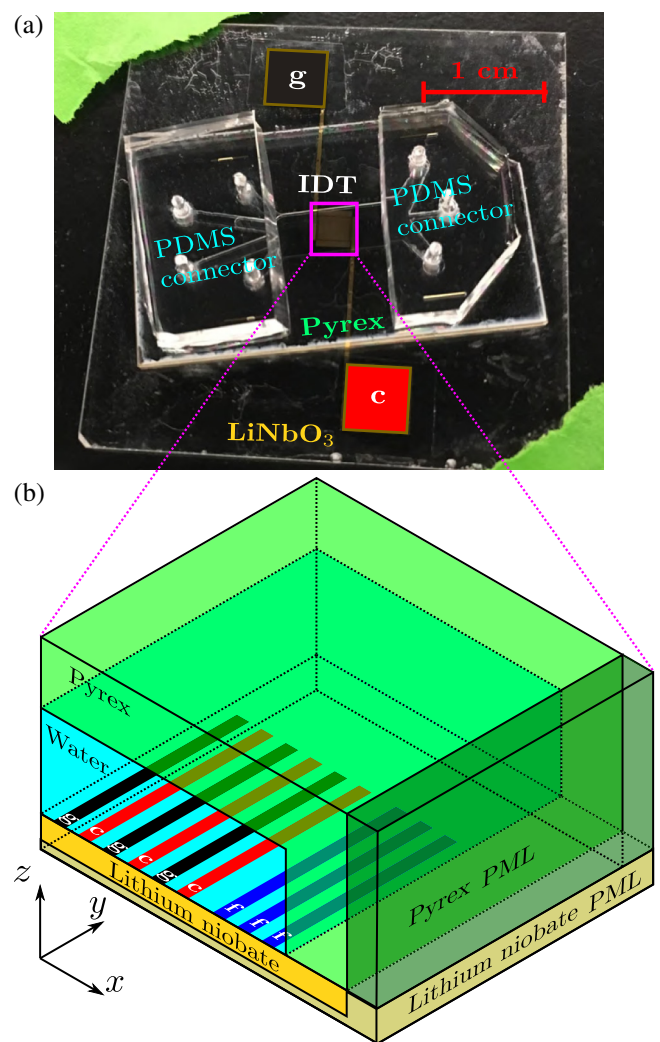


FIG. 1. Experimental and numeric testing devices. (a) Testing device similar to that of Ref. [23]. A wide lithium niobate base with a 24-pair interdigitated surface metal electrode (IDT) and contact pads (grounded, g; charged, c) supports a borosilicate (Pyrex) glass slab containing an etched microchannel above the IDT. (b) 3D sketch of the numerical model, containing only a three-pair electrode (grounded, g, black; charged, c, red) and three floating electrodes (f, blue).

the driving electrodes. As described in more detail in the Appendix, the lattice coordinate system X, Y, Z of the 128° YX-cut lithium niobate wafer is rotated by the usual $38^\circ = 128^\circ - 90^\circ$ about the x axis to obtain an optimal SAW configuration.

To facilitate separation of nanoparticles, the axis of the microchannel is tilted by 10° relative to the IDT electrodes. At both ends, the microchannel branches out into a number of side channels with vertical openings for inlet and outlet tubing. In the numerical model, this inlet and outlet structure is represented by ideally absorbing boundary conditions. The SAW device is actuated by a time-harmonic voltage difference at a frequency f applied to the IDT

electrodes. The corresponding angular frequency is $\omega = 2\pi f$.

The following formulation of the governing equations is a further development of our previous work presented in Refs. [32,35,36] to take into account the SAW in 3D models of lithium niobate-driven ultrasound acoustics in liquid-filled microchannels.

A. The Voigt notation for elastic solids

In linear elastodynamics with an elasticity tensor C_{iklm} , the stress σ_{ik} and strain ϵ_{ik} tensors, with $i, k = 1, 2, 3$ (or x, y, z), are defined in index notation as

$$\epsilon_{ik} = \frac{1}{2} (\partial_i u_k + \partial_k u_i), \quad (1a)$$

$$\sigma_{ik} = C_{iklm} \epsilon_{lm}. \quad (1b)$$

In the Voigt notation (denoted by a subscript V) [37], the symmetric stress and strain double-index tensor components $\sigma_{ik} = \sigma_{ki}$ and $\epsilon_{ik} = \epsilon_{ki}$ are organized into single-index vectors σ_α and ϵ_α , with $\alpha = 1, 2, \dots, 6$, as

$$\epsilon_V = \begin{pmatrix} \epsilon_1 \\ \epsilon_2 \\ \epsilon_3 \\ \epsilon_4 \\ \epsilon_5 \\ \epsilon_6 \end{pmatrix} = \begin{pmatrix} \epsilon_{11} \\ \epsilon_{22} \\ \epsilon_{33} \\ 2\epsilon_{23} \\ 2\epsilon_{13} \\ 2\epsilon_{12} \end{pmatrix}, \quad \sigma_V = \begin{pmatrix} \sigma_1 \\ \sigma_2 \\ \sigma_3 \\ \sigma_4 \\ \sigma_5 \\ \sigma_6 \end{pmatrix} = \begin{pmatrix} \sigma_{11} \\ \sigma_{22} \\ \sigma_{33} \\ \sigma_{23} \\ \sigma_{13} \\ \sigma_{12} \end{pmatrix}, \quad (2a)$$

and the stress-strain relation is written

$$\sigma_\alpha = C_{\alpha\beta} \epsilon_\beta, \quad (3)$$

where $C_{\alpha\beta}$ is the 6×6 Voigt elasticity matrix. We also introduce the 3×6 Voigt matrix gradient operator ∇_V ,

$$\nabla_V = \begin{pmatrix} \partial_x & 0 & 0 & 0 & \partial_z & \partial_y \\ 0 & \partial_y & 0 & \partial_z & 0 & \partial_x \\ 0 & 0 & \partial_z & \partial_y & \partial_x & 0 \end{pmatrix}. \quad (4)$$

The equations governing the device are divided into three sets. One set is the first-order time-harmonic equations

for the acoustic fields, the second set contains the steady time-averaged second-order fields, and the third set is the time-dependent equations describing the acoustophoretic motion of suspended particles.

B. Time-harmonic first-order fields

By construction, all first-order fields are proportional to the time-harmonic electric potential actuating the SAW device at angular frequency ω . Consequently, all first-order fields are time-harmonic acoustic fields of the form $\hat{g}(\mathbf{r}, t) = g(\mathbf{r}) e^{-i\omega t}$, where $g(\mathbf{r})$ is the complex-valued field amplitude. The corresponding physical field is the real part, $\text{Re}[\hat{g}(\mathbf{r}, t)]$. All terms thus have the same explicit time dependence $e^{-i\omega t}$, so this factor is divided out, leaving us with the governing equations for the amplitude g , where for brevity we suppress the spatial argument \mathbf{r} .

In a linear piezoelectric material with a mass density ρ_{sl} and no free charges, the solid displacement field \mathbf{u} and the electric potential field ϕ are governed by the Cauchy equation and Gauss's law,

$$\nabla_V \cdot \sigma_V = -\rho_{\text{sl}} \omega^2 \mathbf{u}, \quad (5a)$$

$$\nabla \cdot \mathbf{D} = 0. \quad (5b)$$

This equation system is closed by the constitutive equations relating the stress σ_V and the electrical displacement \mathbf{D} to the strain ϵ_V and the electric field \mathbf{E} , through the elasticity matrix \mathbf{C} , the relative dielectric tensor ϵ_r , and the piezoelectric coupling matrix \mathbf{e} :

$$\sigma_V = \mathbf{C} \epsilon_V - \mathbf{e}^T \mathbf{E}, \quad \text{with } \mathbf{E} = -\nabla \phi, \quad (5c)$$

$$\mathbf{D} = \epsilon_0 \epsilon_r \mathbf{E} + \mathbf{e} \epsilon_V. \quad (5d)$$

Here, ϵ_0 is the vacuum permittivity, ϵ_r is the relative permittivity tensor of the material, and the superscript T denotes the transpose of a matrix; see Table I.

For anisotropic lithium niobate, Eqs. (5a) and (5b) are turned into equations for \mathbf{u} and ϕ by using the explicit forms of Eqs. (5c) and (5d) written in terms of the coupling matrix,

$$\begin{pmatrix} \sigma_1 \\ \sigma_2 \\ \sigma_3 \\ \sigma_4 \\ \sigma_5 \\ \sigma_6 \\ D_x \\ D_y \\ D_z \end{pmatrix} = \begin{pmatrix} C_{11} & C_{12} & C_{13} & C_{14} & 0 & 0 & 0 & -e_{21} & -e_{31} \\ C_{12} & C_{22} & C_{23} & C_{24} & 0 & 0 & 0 & -e_{22} & -e_{32} \\ C_{13} & C_{23} & C_{33} & C_{34} & 0 & 0 & 0 & -e_{23} & -e_{33} \\ C_{14} & C_{24} & C_{34} & C_{44} & 0 & 0 & 0 & -e_{24} & -e_{34} \\ 0 & 0 & 0 & 0 & C_{55} & C_{56} & -e_{15} & 0 & 0 \\ 0 & 0 & 0 & 0 & C_{56} & C_{66} & -e_{16} & 0 & 0 \\ 0 & 0 & 0 & 0 & e_{15} & e_{16} & \epsilon_{11} & 0 & 0 \\ e_{21} & e_{22} & e_{23} & e_{24} & 0 & 0 & 0 & \epsilon_{22} & \epsilon_{23} \\ e_{31} & e_{32} & e_{33} & e_{34} & 0 & 0 & 0 & \epsilon_{23} & \epsilon_{33} \end{pmatrix} \begin{pmatrix} \epsilon_1 \\ \epsilon_2 \\ \epsilon_3 \\ \epsilon_4 \\ \epsilon_5 \\ \epsilon_6 \\ E_x \\ E_y \\ E_z \end{pmatrix}. \quad (6a)$$

For isotropic elastic solids with no charges and no piezoelectric coupling, $\mathbf{e} = \mathbf{0}$, and only Eq. (5a) is relevant; it becomes an equation for \mathbf{u} , as Eq. (5c) reduces to

$$\begin{pmatrix} \sigma_1 \\ \sigma_2 \\ \sigma_3 \\ \sigma_4 \\ \sigma_5 \\ \sigma_6 \end{pmatrix} = \begin{pmatrix} C_{11} & C_{12} & C_{12} & 0 & 0 & 0 \\ C_{12} & C_{11} & C_{12} & 0 & 0 & 0 \\ C_{12} & C_{12} & C_{11} & 0 & 0 & 0 \\ 0 & 0 & 0 & C_{44} & 0 & 0 \\ 0 & 0 & 0 & 0 & C_{44} & 0 \\ 0 & 0 & 0 & 0 & 0 & C_{44} \end{pmatrix} \begin{pmatrix} \epsilon_1 \\ \epsilon_2 \\ \epsilon_3 \\ \epsilon_4 \\ \epsilon_5 \\ \epsilon_6 \end{pmatrix}, \quad (6b)$$

with only two independent elastic constants, C_{11} and C_{44} , because $C_{12} = C_{11} - 2C_{44}$ for an isotropic material.

In a fluid with speed of sound c_{fl} , mass density ρ_{fl} , dynamic viscosity η_{fl} , viscous boundary-layer thickness $\delta = \sqrt{2\eta_{\text{fl}}/\rho_{\text{fl}}\omega}$, viscosity ratio $\beta = \eta_{\text{fl}}^b/\eta_{\text{fl}} + \frac{1}{3}$, and effective damping coefficient $\Gamma_{\text{fl}} = [(1 + \beta)/2](k_0\delta)^2$, the first-order pressure field p_1 is governed by the Helmholtz equation, and the acoustic velocity field \mathbf{v}_1 is given by the pressure gradient:

$$\nabla \cdot (\nabla p_1) = -k_c^2 p_1, \quad \text{with } k_c = \frac{\omega}{c_{\text{fl}}} \left(1 + i\frac{\Gamma_{\text{fl}}}{2}\right), \quad (7a)$$

TABLE I. Elastic constants $C_{\alpha\beta}$, mass density ρ_{sl} , piezoelectric coupling constants $e_{i\alpha}$, and relative dielectric constants ϵ_{ik} of the materials used in this work. The values for 128° YX-cut lithium niobate are defined in the global system x, y, z ; for derivations, see the Appendix. Note that $C_{12} = C_{11} - 2C_{44}$ for isotropic materials (Pyrex and PDMS here).

Parameter	Value	Parameter	Value
128° YX-cut lithium niobate [38]			
C_{11}	202.89 GPa	C_{12}	72.33 GPa
C_{13}	60.17 GPa	C_{14}	10.74 GPa
C_{22}	194.23 GPa	C_{23}	90.59 GPa
C_{24}	8.97 GPa	C_{33}	220.29 GPa
C_{34}	8.14 GPa	C_{44}	74.89 GPa
C_{55}	72.79 GPa	C_{56}	+8.51 GPa
ρ_{sl}	4628 kg m ⁻³	C_{66}	59.51 GPa
e_{15}	0.10 C m ⁻²	e_{16}	-6.09 C m ⁻²
e_{21}	-1.73 C m ⁻²	e_{22}	4.48 C m ⁻²
e_{23}	-1.67 C m ⁻²	e_{24}	0.14 C m ⁻²
e_{31}	1.64 C m ⁻²	e_{32}	-2.69 C m ⁻²
e_{33}	2.44 C m ⁻²	e_{34}	0.55 C m ⁻²
ϵ_{11}	44.30	ϵ_{22}	38.08
ϵ_{23}	-7.96	ϵ_{33}	34.12
Pyrex [39]			
C_{11}	69.73 GPa	C_{12}	17.45 GPa
ρ_{sl}	2230 kg m ⁻³	C_{44}	26.14 GPa
ϵ	4.6	Γ_{sl}	0.0002
PDMS [40–42]			
C_{11}	1.13 GPa	C_{12}	1.11 GPa
ρ_{sl}	1070 kg m ⁻³	C_{44}	0.011 GPa
ϵ	2.5	Γ_{sl}	0.0213

$$\mathbf{v}_1 = \frac{-i}{\omega\rho_{\text{fl}}} (1 - i\Gamma_{\text{fl}}) \nabla p_1, \quad (7b)$$

where k_c is the weakly damped compressional wave number [43]. See Table II for parameter values.

Turning to the boundary conditions, we introduce \mathbf{n} as the normal vector to a given surface. The SAW device in Fig. 1 is actuated by a time-harmonic potential of amplitude V_0 on the surfaces of the charged electrodes (CE) and 0 V on the grounded electrodes (GE), respectively:

$$\phi_{\text{CE}} = V_0 e^{-i\omega t}, \quad \phi_{\text{GE}} = 0. \quad (8a)$$

Our study is valid for the time-harmonic state that the system reaches after the transient phase that is initiated by turning on the driving voltage. As analyzed in Ref. [45], the time-harmonic state is reached after about 10 000 oscillation periods, corresponding to 0.2 ms. A given floating electrode (FE) is modeled as an ideal equipotential domain with a vanishing tangential electrical field on its surface:

$$(\mathbf{I} - \mathbf{nn}) \cdot \nabla \phi_{\text{FE}} = \mathbf{0}, \quad (8b)$$

where \mathbf{I} is the unit tensor, and $(\mathbf{I} - \mathbf{nn})$ is the usual tangent projection tensor. Note that this condition is automatically enforced on any surface with a spatially invariant Dirichlet condition applied along it. Note also that the value of the potential on each floating electrode is *a priori* unknown and must be determined self-consistently from the governing equations and boundary conditions.

At a given fluid-solid interface, we impose the usual continuity conditions [32] with the recently developed boundary-layer corrections included [43]: the solid stress σ_{sl} is given by the acoustic pressure p_1 with the addition of

TABLE II. Material parameters of water, from Ref. [44].

Parameter	Symbol	Value
Speed of sound	c_{fl}	1497 m s ⁻¹
Mass density	ρ_{fl}	997 kg m ⁻³
Dynamic viscosity	η_{fl}	0.89 mPa s
Bulk viscosity	η_{fl}^b	2.485 mPa s
Compressibility	κ_{fl}	452 TPa ⁻¹

the boundary-layer stress, and the fluid velocity \mathbf{v}_1 is given by the solid-wall velocity $\mathbf{v}_{sl} = -i\omega\mathbf{u}$ with the addition of the boundary-layer velocity $\mathbf{v}_{sl} - \mathbf{v}_1$,

$$\boldsymbol{\sigma}_{sl} \cdot \mathbf{n} = -p_1 \mathbf{n} + ik_s \eta_{fl} (\mathbf{v}_{sl} - \mathbf{v}_1), \quad (9a)$$

$$\mathbf{n} \cdot \mathbf{v}_1 = \mathbf{n} \cdot \mathbf{v}_{sl} + \frac{i}{k_s} \nabla_{\parallel} \cdot (\mathbf{v}_{sl} - \mathbf{v}_1), \quad (9b)$$

$$\text{with shear wave number } k_s = \frac{1+i}{\delta}. \quad (9c)$$

The terms containing the shear wave number k_s represent the corrections arising from taking the 400 nm-wide viscous boundary layer into account analytically [43].

All exterior solid surfaces facing the air have a stress-free boundary condition prescribed,

$$\boldsymbol{\sigma} \cdot \mathbf{n} = \mathbf{0}. \quad (10)$$

This is a good approximation because the surrounding air has an acoustic impedance 3–4 orders of magnitude lower than that of the solids used, causing 99.99% of the incident acoustic waves from the solids to be reflected. Moreover, the shear stress from the air is negligible.

C. Time-averaged second-order fields

The slow-timescale or steady fields in the fluid are the time-averaged second-order velocity field \mathbf{v}_2 and pressure field p_2 . These are governed by the time-averaged momentum- and mass-conservation equations,

$$\nabla \cdot \boldsymbol{\sigma}_2 - \rho_0 \nabla \cdot \langle \mathbf{v}_1 \mathbf{v}_1 \rangle = \mathbf{0}, \quad (11a)$$

$$\nabla \cdot (\rho_0 \mathbf{v}_2 + \langle \rho_1 \mathbf{v}_1 \rangle) = 0, \quad (11b)$$

where $\boldsymbol{\sigma}_2$ is the second-order stress tensor of the fluid,

$$\boldsymbol{\sigma}_2 = -p_2 \mathbf{I} + \eta [\nabla \mathbf{v}_2 + (\nabla \mathbf{v}_2)^T] + (\beta - 1) \eta (\nabla \cdot \mathbf{v}_2) \mathbf{I}. \quad (11c)$$

Along a fluid-solid interface with tangential vectors \mathbf{e}_{ξ} and \mathbf{e}_{η} and normal vector $\mathbf{e}_{\zeta} = \mathbf{n}$, we use the effective boundary condition derived in Ref. [43] for \mathbf{v}_2 . Here, the viscous boundary layer is taken into account analytically by introducing the boundary-layer velocity field $\mathbf{v}^{\delta 0} = \mathbf{v}_{sl} - \mathbf{v}_1$ in the fluid along the fluid-solid interface,

$$\mathbf{v}_2 = (\mathbf{A} \cdot \mathbf{e}_{\xi}) \mathbf{e}_{\xi} + (\mathbf{A} \cdot \mathbf{e}_{\eta}) \mathbf{e}_{\eta} + (\mathbf{B} \cdot \mathbf{e}_{\zeta}) \mathbf{e}_{\zeta}, \quad (12a)$$

$$\mathbf{A} = -\frac{1}{2\omega} \text{Re} \left\{ \mathbf{v}_1^{\delta 0*} \cdot \nabla \left(\frac{1}{2} \mathbf{v}_1^{\delta 0} - i \mathbf{v}_{sl} \right) - i \mathbf{v}_{sl}^* \cdot \nabla \mathbf{v}_1 + \left[\frac{2-i}{2} \nabla \cdot \mathbf{v}_1^{\delta 0*} + i (\nabla \cdot \mathbf{v}_{sl}^* - \partial_{\zeta} v_{1\zeta}^*) \right] \mathbf{v}_1^{\delta 0} \right\}, \quad (12b)$$

$$\mathbf{B} = \frac{1}{2\omega} \text{Re} \left\{ i \mathbf{v}_1^* \cdot \nabla \mathbf{v}_1 \right\}, \quad (12c)$$

where the asterisk denotes complex conjugation.

D. Acoustophoresis of suspended particles

To predict the acoustophoretic motion of a dilute suspension of spherical micrometer- and submicrometer-sized particles in a fluid of density ρ_{fl} , compressibility κ_{fl} , and viscosity η_{fl} , we implement a particle-tracing routine in the model. We consider Newton's second law for a single spherical particle of radius a_{pt} and density ρ_{pt} moving with velocity \mathbf{v}_{pt} under the influence of gravity \mathbf{g} , the acoustic radiation force \mathbf{F}^{rad} [46], and the Stokes drag force \mathbf{F}^{drag} [47] induced by acoustic streaming of the fluid,

$$\frac{4\pi}{3} a_{pt}^3 \rho_{pt} \frac{d\mathbf{v}_{pt}}{dt} = \rho_{pt} \mathbf{g} + \mathbf{F}^{\text{rad}} + \mathbf{F}^{\text{drag}}, \quad (13a)$$

$$\mathbf{F}^{\text{rad}} = -\frac{4}{3} \pi a^3 \left[\kappa_{fl} \langle (f_0 p_1) \nabla p_1 \rangle - \frac{3}{2} \rho_{fl} \langle (f_1 \mathbf{v}_1) \cdot \nabla \mathbf{v}_1 \rangle \right], \quad (13b)$$

$$\mathbf{F}^{\text{drag}} = 6\pi a \eta_{fl} (\mathbf{v}_2 - \mathbf{v}_{pt}). \quad (13c)$$

Here, $f_0 = 0.444$ and $f_1 = 0.034$ are the monopole and dipole scattering coefficients of the suspended particles at 50 MHz, where the values are for polystyrene micro- and nanoparticles in water [48]. When studying different particle sizes, it is convenient to introduce the radiation force density \mathbf{f}^{rad} ,

$$\mathbf{f}^{\text{rad}} = \frac{3}{4\pi a^3} \mathbf{F}^{\text{rad}}. \quad (13d)$$

By direct time integration of Eq. (13a) applied to a set of particles initially placed on a square grid, the acoustophoretic motion of the particles can be predicted and compared with the experimentally observed motion. We note that the effects of gravity are negligible, as $\rho_{pt} \mathbf{g} \ll \kappa_{fl} \langle (f_0 p_1) \nabla p_1 \rangle$.

III. NUMERICAL IMPLEMENTATION

Inspired by previous experimental work of Sehgal and Kirby [23], we study the SAW test system shown in Fig. 1, with actuating electrodes and Bragg-reflector electrodes placed directly underneath the microchannel. The parameter values used in the numerical simulation are listed in Table III, and a sketch of the vertical cross section of the test system is shown in Fig. 2. Note that the SAW wavelength λ_{SAW} is set by the IDT electrode geometry as $\lambda_{\text{SAW}} = 2(W_{el} + G_{el})$. We study microcavities defined in

TABLE III. Dimensions in the numeric 2D and 3D models.

Parameter	Symbol	2D	3D	Units
Device depth (y)	L_{sl}		1200	μm
Solid height (z)	H_{sl}	40–1000	500	μm
Solid width (x)	W_{sl}	200	80	μm
Channel height	H_{fl}	50–200	50	μm
Channel width	W_{fl}	3500	900	μm
Piezo height	H_{pz}	100–500	300	μm
PML length	L_{PML}	80	80	μm
Electrode depth (y)	L_{el}		400	μm
Electrode height (z)	H_{el}	0.4	0.4	μm
Electrode width (x)	W_{el}	20	20	μm
Electrode gap	G_{el}	20	20	μm
SAW wavelength	λ_{SAW}	80	80	μm
No. of electrode pairs	n_{el}	24	4	
No. of reflectors	n_{rf}	0–6	0	
Actuation frequency	f_0	30–60	50	MHz
Driving voltage	V_0	1	1	V
Degrees of freedom	n_{DOF}	$\mathcal{O}(10^5)$	$\mathcal{O}(10^6)$	
Memory requirements	R	$\mathcal{O}(10)$	$\mathcal{O}(10^3)$	GB

either acoustically soft PDMS [see Fig. 2(a)] or acoustically hard borosilicate (Pyrex) glass [see Fig. 2(b)], and we perform numerical simulation in both two and three dimensions.

Following the procedure of our previous numerical simulations [32,36], the coupled governing equations in Secs. II B–II D are implemented in the finite-element-method software package COMSOL Multiphysics 5.3a [49], using the weak-form partial differential equation interface ‘‘PDE Weak Form’’ in the mathematics module. For a given driving voltage V_0 , actuation frequency f , and angular frequency $\omega = 2\pi f$ specified in the actuation boundary condition (8a), the numeric model is solved in three sequential steps: (1) the first-order equations (5) and (7a) presented in Sec. II B for the pressure p_1 , displacement \mathbf{u} , and electric potential ϕ , together with the corresponding boundary conditions Eqs. (8)–(10); (2) the steady second-order streaming velocity \mathbf{v}_2 presented in Sec. II C governed by Eqs. (11) and (12), where time-averaged products of the first-order fields appear as source terms; and (3) the acoustophoretic motion of suspended test particles presented in Sec. II > D found by time integration of Eq. (13).

Simulations of the full 3D model are time- and computer-memory-consuming. Therefore, part of the analysis is performed on 2D models to study the resonance behavior of the device and the acoustic radiation force in the vertical y - z plane normal to the electrodes in the horizontal x - y plane. In these simulations, presented in Sec. V, it is possible to model a cross section of the device to scale. To investigate effects that have nontrivial behavior in the full three dimensions, such as acoustic streaming and the acoustophoretic motion of suspended particles presented in Sec. V, we must perform full 3D modeling. However,

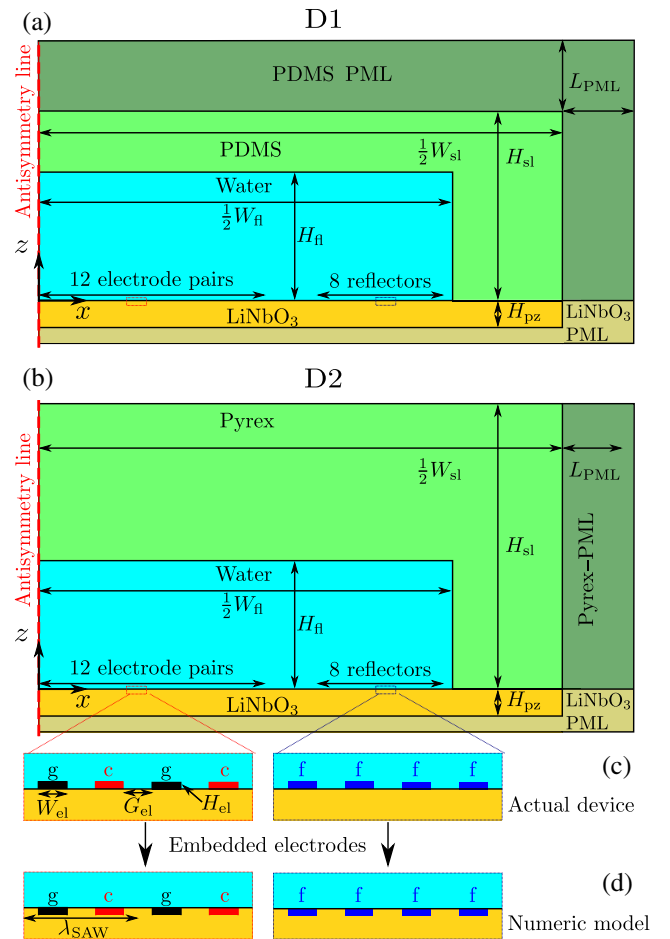


FIG. 2. Vertical 2D cross section of the numeric model and illustration of the embedded electrodes used in the simulations, with (a) a highly attenuating low-reflection polymer PDMS lid as used in Ref. [23], and (b) a stiff acoustically reflecting Pyrex glass lid. (c) The 12 pairs of grounded (g, black) and charged (c, red) electrodes, as well as the floating (f, blue) electrodes, are all included with their entire height, but in (d) they are lowered into the lithium niobate (yellow) to be level with the substrate. Note that $\lambda_{SAW} = 2(W_{el} + G_{el})$.

in this case, the extended computer-memory requirements necessitate a scaling down of the model. The parameters for the 2D and 3D simulations are listed in Table III.

As in previous work [32], we perform convergence analyses of the model to verify that the model converges towards a single solution as the mesh size decreases. We use a cubic-order test function with the following resolution in each domain, given in nodes per wavelength (NPW). In the 2D simulations, the lithium niobate has 72 NPW laterally and 12 NPW vertically, the Pyrex has 25 NPW laterally and 25 NPW vertically, the PDMS has 10 NPW laterally and 10 NPW vertically, and the water has 160 NPW laterally and 19 NPW vertically. In the 3D simulations, the lithium niobate has 10 NPW laterally and 9 NPW vertically, the Pyrex has 12 NPW laterally and 12

NPW vertically, and the water has 22 NPW laterally and 6 NPW vertically.

A. Perfectly matched layers

We reduce the numeric footprint of the model by implementing perfectly matched layers (PMLs) in the model, as described by Ley and Bruus [32]: large passive domains surrounding the acoustically active region are replaced by much smaller domains, in which PMLs act as ideal absorbers of outgoing acoustic waves, thus completely removing reflections. In contrast to Ref. [32], the PMLs in the present model are functions of all three spatial coordinates.

In the small surrounding domains, the PMLs are implemented in the weak-form governing equations by a complex-valued coordinate transformation of the spatial derivatives ∂x_i and integral measures dx_i that appear:

$$\partial x_i \rightarrow \partial \tilde{x}_i = \frac{1}{1 + i s(\mathbf{r})} \partial x_i, \quad (14a)$$

$$dx_i \rightarrow d\tilde{x}_i = [1 + i s(\mathbf{r})] dx_i, \quad (14b)$$

$$s(\mathbf{r}) = k_{\text{PML}} \sum_{i=x,y,z} \frac{(x_i - x_{0i})^2}{L_{\text{PML},i}^2} \Theta(x_i - x_{0i}), \quad (14c)$$

where $s(\mathbf{r})$ is a real-valued function of position. Here, $s(\mathbf{r})$ is given for the specific case shown in Fig. 2 with a PML of width $L_{\text{PML},i}$ in the three coordinate directions $i = x, y, z$ placed outside the region $x < x_0, y < y_0$, and $z < z_0$; $\Theta(x)$ is the Heaviside step function ($= 1$ for $x > 0$, and 0 otherwise); and k_{PML} is an adjustable parameter for the strength of the PML absorption. The bottom PML in the niobate substrate is used because SAWs decay exponentially in depth on the scale of the wavelength, whereas the top and side PMLs are used to mimic attenuation in the respective materials over large distances.

B. Symmetry planes

As in previous numeric work [32,45], we use an antisymmetry line to reduce the numerical cost of our 2D models. The antisymmetry line is realized by boundary conditions on the solid displacement, the electric potential, and the fluid pressure along the line:

$$\partial_x u_x = 0, \quad (15a)$$

$$u_z = 0, \quad (15b)$$

$$\phi = \frac{1}{2} V_0, \quad (15c)$$

$$p_1 = 0. \quad (15d)$$

We check these conditions against the values along the device centerline in a 2D simulation for a fully symmetric device and observe that they are in good agreement.

In three dimensions we cannot use symmetry planes, as the device is manifestly asymmetric due to the 10° angle between the IDT and the walls of the microchannel.

C. Embedded electrodes

In the actual device, the 400-nm-thick electrodes protrude into the fluid domain. In our numeric model, we simplify the device by submerging them in the substrate to form a planar solid-fluid interface, as shown in Fig. 2. Thereby, the fluid-solid interface has no sharp corners, at which singularities would appear in the numeric gradients. Furthermore, the planar interface mitigates the need for an enormous number of mesh elements ranging from nanometers to micrometers in size in the fluid domain, which would either lower the element quality greatly or add massive computational cost. This reduction in model complexity is justified by the height of the electrodes being less than 1% of the channel height and having no influence on the pressure acoustics of the system. On the other hand, we cannot completely neglect the electrodes, because jumps in acoustic impedance between the metal electrodes and the niobate substrate cause partial reflections of SAWs running along the substrate. Thus we choose to keep the electrodes but submerge them. For a smaller section of the device, we numerically compare the response to embedded versus unembedded electrodes in 2D simulations. The overall response is the same when a sufficiently high spatial resolution is used near the corners of the unembedded electrodes, but we find an increased streaming velocity near the electrode corners.

IV. EXPERIMENTAL METHODS

To validate the numerical models, we perform experiments on two type of device, listed in Table IV, namely microchannels defined in slabs of either PDMS (D1) or Pyrex (D2) bonded on top of a lithium niobate substrate equipped with an IDT and Bragg reflectors. The PDMS device (D1) is fabricated by standard photolithography techniques, listed in our previous paper [23]. The Pyrex device (D2) is fabricated by glass microfabrication techniques, briefly described in the following. A microchannel of the desired dimensions is wet-etched in a borosilicate glass wafer with 49% hydrofluoric acid using a multilayered mask of chrome, gold, and SPR220 photoresist. The input and output ports of the microchannel are obtained by

TABLE IV. The devices D1 and D2 used in the experimental validation of the numerical model, which differ in the choice of lid. The other parameters of D1 and D2 are listed in Table III.

Device	Lid material	Lid thickness (mm)
D1	PDMS	15
D2 [see Fig. 1(a)]	Pyrex	0.45

laser cutting of the glass. The bonding between the glass microchannel and the lithium niobate substrate is achieved by coating a $5\ \mu\text{m}$ layer of SU-8 epoxy onto the surface of the lithium niobate. The microchannel is gently placed on the uncured SU-8 and the epoxy is baked following standard steps. The SU-8 outside the microchannel region is selectively cross-linked to achieve bonding, and the SU-8 inside the microchannel region is dissolved away with a developer, thus obtaining a Pyrex-lid microchannel on top of the lithium niobate substrate. The devices are tested with $1.7\text{-}\mu\text{m}$ -diameter fluorescent polystyrene particles (Polysciences, Inc.) suspended in deionized water ($18.2\ \text{M}\Omega/\text{cm}$, Labconco WaterPro PS) containing 0.7% (w/v) Pluronic F-127 to prevent particle aggregation. The particle solution is injected into the microchannel after priming the device with 70% ethanol solution to avoid the formation of air bubbles. An ultrasound field is set up in the device by applying an RF signal at the desired frequency to the IDT with a HP 8643A signal generator and an ENI 350L RF power amplifier. The acoustophoretic motion of the tracer particles is visualized with a fixed-stage upright fluorescent microscope (Olympus BX51WI) with a digital CCD camera (Retiga 1300, Q Imaging). The images are acquired with the Q-Capture Pro 7 software package and postprocessed in ImageJ. The electrical impedance of the devices is measured directly with an impedance analyzer (Agilent 4395A).

V. RESULTS OF 2D MODELING

In the following, we compare the results of the 2D modeling in the vertical x - z plane with experiments carried out on the two devices D1 and D2 listed in Table IV. Such a comparison is reasonable because the low channel height of $50\ \mu\text{m}$ implies an approximate translation invariance along the y axis spanning the length (aperture), $2400\ \mu\text{m}$, of the IDT electrodes, as seen in the 3D geometry of Fig. 1. Also, the variation along the x axis, given by the width $20\ \mu\text{m}$ of the individual electrodes, and the periodicity $\lambda_{\text{SAW}} = 80\ \mu\text{m}$ of the IDT are much smaller than the IDT aperture along the y axis. We can therefore obtain a reasonable estimate of the electrical and acoustical response of the device by just considering the 2D domain in the vertical x - z plane shown in Fig. 2.

A. Electrical response

As a first validation of the model, we study the electrical impedance

$$Z^{\text{el}} = |Z^{\text{el}}| e^{-i\psi} = \frac{V_0}{I} \quad (16)$$

in terms of the driving voltage V_0 and the complex-valued current I through the device, because this quantity is relatively easy to obtain both in the simulation and in the

experiment. We compare the model predictions of the magnitude $|Z^{\text{el}}|$ and phase ψ of the impedance with their experimentally measured counterparts.

In the model, we compute Z^{el} from the time-harmonic dielectric polarization density \mathbf{P} and the corresponding polarization current \mathbf{J}_{pol} in the lithium niobate substrate, which we treat as an ideal dielectric without free charges:

$$\mathbf{P} = \mathbf{D} - \varepsilon_0 \mathbf{E}, \quad (17a)$$

$$\mathbf{J}_{\text{pol}} = -i\omega \mathbf{P}. \quad (17b)$$

The total current I through the device is given by the surface integral of \mathbf{J}_{pol} over one of the charged electrodes with potential $\phi_{\text{CE}} = V_0$ and surface $\partial\Omega_{\text{CE}}$,

$$I = \int_{\partial\Omega_{\text{CE}}} \mathbf{J}_{\text{pol}} \cdot \mathbf{n} dA. \quad (17c)$$

The modulus $|Z^{\text{el}}|$ and phase angle $\psi = \arg(Z^{\text{el}})$ are thus

$$|Z^{\text{el}}| = \left| \frac{V_0}{I} \right|, \quad \psi = \arg\left(\frac{V_0}{I}\right). \quad (17d)$$

In Figs. 3(a) and 3(b), we compare the values of $|Z^{\text{el}}|$ computed from Eq. (17d) for our 2D model with those measured on the Pyrex device D2, shown in Fig. 1(a) and listed in Table IV, for microchannels containing air

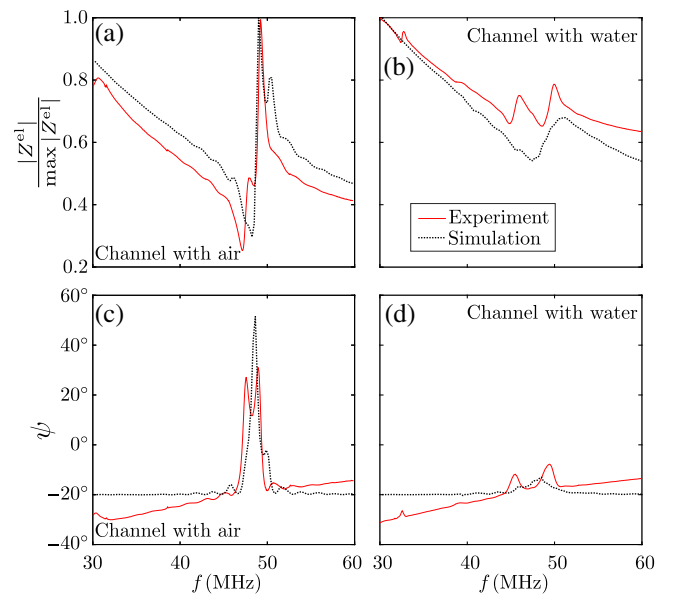


FIG. 3. Line plots of the normalized magnitude $|Z^{\text{el}}|$ and phase ψ of the electrical impedance Z^{el} as functions of frequency, determined by experiment (full red line) and by numerical simulation (dotted black line). The measurements and simulations are carried out for a microchannel containing either vacuum or deionized water.

TABLE V. Measured and simulated values of the frequencies f near the ideal (unloaded) frequency $f_{\text{SAW}} = 49.9$ MHz, where $|Z^{\text{el}}(f)|$ and $\psi(f)$ have local minima and maxima in the Pyrex device D2.

Extremum	f_{exp} (GHz)	f_{num} (GHz)	Relative error (%)
A	47.35	48.25	1.9
B	48.05	49.00	2.0
C	49.40	50.25	1.7
D	48.65	47.50	1.7
E	50.00	50.75	1.7
F	47.70	48.75	2.2
G	49.10	50.00	1.8
H	45.50	46.00	1.1
I	49.40	48.50	1.8

or deionized water. The numerical simulation predicts correctly the value of the resonance observed near 48 MHz in the experiments. As shown in Table V, the relative difference between the computed and measured values of the frequencies f where $|Z^{\text{el}}(f)|$ and $\psi(f)$ have local minima or maxima is about 2% or less. We also see that the simulation also predicts the monotonically decreasing background signal for $|Z^{\text{el}}(f)|$ before and after the resonance relatively well, for both an air- and a water-filled microchannel. However, the simulation fails to predict the correct ratio of the resonance peak heights.

For the phase ψ , shown in Figs. 3(c) and 3(d), the simulation predicts the resonance frequencies correctly, but fails to predict the monotonically increasing background signal. By adding external stray impedances to our 2D model to simulate the surrounding 3D system, however, it is possible to generate a slant in the phase curves by fitting the values of these stray impedances. We do not show these results, as they are descriptive and not predictive in nature.

B. Wall material: Hard Pyrex versus soft PDMS

Our previous device [23] features a soft PDMS-polymer lid, as is commonly used due to the ease of fabrication and handling. However, the acoustic properties of PDMS are far from ideal: its impedance is nearly equal to that of water (20% lower), and the attenuation is about two orders of magnitude larger than that of the boundary layer in water. In the following, we therefore simulate the acoustic properties of device D1, with a PDMS lid, and contrast them with those of device D2, with a much stiffer Pyrex lid, using the two models shown in Fig. 2 and listed in Table IV. Compared with water, the acoustic impedance of Pyrex is 8.3 times larger and its attenuation 10 times smaller. We neglect the 5- μm -thick SU-8 bonding layer as it is not present in the water domain and the IDT-electrode area, where most of the acoustic energy couples into the system. Moreover, the SU-8 layer is 100 times thinner than

the Pyrex slab, and its acoustic impedance is only 4 times less than that of Pyrex.

We study by numerical simulation the acoustic fields in devices D1 and D2 near the ideal (unloaded) frequency $f_{\text{SAW}} = 49.9$ MHz. By locating the maximum of the average acoustic energy in the water-filled channel when plotted versus the actuation frequency f (not shown), we determine the (loaded) resonance frequency f_{res} of the two devices to be $f_{\text{res}}^{\text{D1}} = 47.75$ MHz and $f_{\text{res}}^{\text{D2}} = 46.50$ MHz, respectively. In Fig. 4, we show line plots along the height (z direction) and across the width (x direction) of numerically simulated acoustic fields for these two devices.

Figures 4(a) and 4(b) show the magnitude $|u_z|$ of the z component of the acoustic displacement \mathbf{u} , which in water is defined through the acoustic velocity Eq. (7b) as

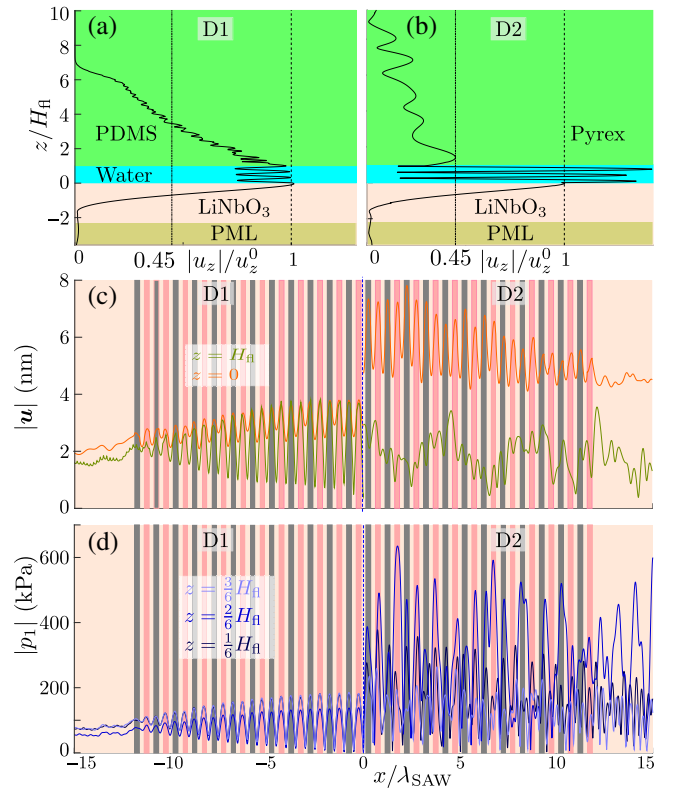


FIG. 4. Amplitude of the displacement $|\mathbf{u}|$ and pressure amplitude $|p_1|$ in the PDMS-lid device D1 and in the Pyrex-lid device D2 at their respective resonance frequencies $f_{\text{res}}^{\text{D1}} = 47.75$ MHz and $f_{\text{res}}^{\text{D2}} = 46.50$ MHz at $V_0 = 1$ V. (a) Line plot of the z component $|u_z|$ along the vertical line $x = W_{c1}$ (the center of the middle electrode) from the bottom of the substrate (beige), through the water (blue), to the top of the PDMS lid (green). (b) As in (a), but for the Pyrex-lid device D2. (c) Line plot of $|u|$ along the top ($z = H_{fl}$) and bottom ($z = 0$) of the channel in D1 ($x < 0$) and in D2 ($x > 0$). The dark gray and pink rectangles for $-12 < x/\lambda_{\text{SAW}} < 12$ represent the IDT electrodes. (d) As in panel (c), but for $|p_1|$ along the horizontal lines at $z/H_{fl} = \frac{3}{6}, \frac{2}{6},$ and $\frac{1}{6}$ inside the channel.

$\mathbf{v}_1 = -i\omega \mathbf{u}$, along a vertical cut line through the entire device. In D1, $|u_z|$ has the characteristics of a traveling wave emitted from the SAW substrate (with maximum amplitude), traversing the water with little reflection (a small oscillation amplitude), and being absorbed in the PDMS lid (decaying amplitude). In contrast, $|u_z|$ in D2 has the characteristics of a standing wave localized in the water channel with reflections from the surrounding solids: huge oscillations in the water domain, with minima close to zero and an amplitude exceeding that in the emitting substrate and the receiving lid. We also notice that in the stiff Pyrex the attenuation is weak, and that the wave is reminiscent of a standing wave between the water interface below the lid and the air interface above. The corresponding acoustic energy flux density $\mathbf{S}_{ac} = \langle p_1 \mathbf{v}_1 \rangle$ in both systems is nonzero and predominantly vertical, but with a much larger amplitude in D1 than in D2.

Figure 4(c) shows the magnitude $|\mathbf{u}|$ of the acoustic displacement \mathbf{u} along horizontal cut lines following the top ($z = H_{fl}$) and the bottom ($z = 0$) of the water channel across the region containing the IDT. In both devices the periodicity of the IDT electrodes is clearly seen, but the amplitude in the nearly standing-wave case of D2 is 2–3 times larger than in the traveling-wave case of D1. Moreover, it is seen that the acoustic waves dies out faster in D1 than in D2 away from the IDT region. The tiny oscillations in the PDMS lid (green curve) for $x < -12\lambda_{SAW}$ stem from the minute transverse wavelength $\sim 11 \mu\text{m} = 0.13\lambda_{SAW}$ in PDMS.

Figure 4(d) shows the magnitude $|p_1|$ of the acoustic pressure p_1 in the water along the horizontal cut lines $z/H_{fl} = \frac{1}{6}, \frac{2}{6},$ and $\frac{3}{6}$. Here the traveling-versus-standing-wave nature of the two devices mentioned above is prominent: In D1, $|p_1|$ is nearly independent of the height, and its envelope amplitude decays steadily from 90 to 55 kPa from the center to the edge of the IDT region. In contrast, $|p_1|$ has large amplitude fluctuations as a function of the horizontal position x and for the three vertical z positions. Moreover, $|p_1|$ does not decay away from the IDT. Clearly, p_1 in the water channel of D2 is dominated by reflections between the solid-water interfaces. This observation can be quantified by the standing-wave ratio, $R = \max(|p_1|)/\min(|p_1|)$, which describes the ratio of standing to traveling waves in a given field. In an ideal resonator and in an ideally transmitting system, $R = \infty$ and 1, respectively. Here, we find $R(\text{D2}) = 12.7$ and $R(\text{D1}) = 1.3$. These numbers underline the good acoustic properties of the water-Pyrex system compared with the bad properties of the PDMS system. The ratio of the R numbers is 9.8, almost equal to the impedance ratio 10.5, which emphasizes the nearly perfect vertical energy flux density \mathbf{S}_{ac} discussed above, obtained as the impedance extracted from the properties of a plane wave with a vertical incident on a planar surface.

C. Acoustophoresis

Although we do not perform an experimental validation of the above simulation results for the acoustic fields p_1 and \mathbf{u} , we compare in the following the experimentally observed acoustophoretic motion of microparticle suspensions in the water-filled microchannel at the SAW resonance frequency f_{SAW} with that obtained by numerical simulation in our 2D model. The central experimental and numerical results are shown in Fig. 5, in the left column for the PDMS-lid device D1 and in the right column for the Pyrex-lid device D2. In the Supplemental Material [50], four animations of the acoustophoresis of 0.1- μm - and 1.7- μm -diameter particles in devices D1 and D2 [Figs. 5(c) and 5(g)] are shown.

In Figs. 5(a) and 5(e), we observe that the suspended 1.7- μm -diameter particles in D1 focus on the edges of the electrodes, whereas in D2 they mainly focus along the centerline of each electrode. This difference in acoustophoretic focusing is caused solely by the choice of lid material and its thickness. Earlier, in Fig. 4, we saw how the change from the PDMS lid to the Pyrex lid led to a change from a predominantly traveling wave to a nearly standing wave in the z direction. As a consequence, both the pressure and its gradients in device D1 are smaller than those in D2, and it follows from Eq. (13b) that the acoustic radiation force \mathbf{F}^{rad} changes significantly.

This change in \mathbf{F}^{rad} per particle volume, denoted by \mathbf{f}^{rad} in Eq. (13d), is shown as vector and gray-scale plots for devices D1 and D2 in the right halves of Figs. 5(b) and 5(f), respectively. Compared with D2, which has $|\mathbf{f}^{rad}| = 7.4 \text{ pN}/\mu\text{m}^3$, the magnitude $|\mathbf{f}^{rad}| = 0.4 \text{ pN}/\mu\text{m}^3$ is 18 times smaller in D1, and $|\mathbf{f}^{rad}|$ is more smeared out (with even smaller gradients). Both force fields have a three-period structure along the vertical z axis, reflecting the fact that $H_{fl} \approx \frac{3}{2}c_{fl}/f_{SAW}$. In D1, the center of the force-field structure is displayed relative to the center of the electrode, whereas in D2 it is above the electrode center. Moreover, whereas \mathbf{f}^{rad} has four less-marked unstable nodal planes in D1 at $z/H_{fl} = 0, \frac{1}{3}, \frac{2}{3}, 1$, it has three well-defined stable ones in D2 at $z/H_{fl} = \frac{1}{6}, \frac{3}{6}, \frac{5}{6}$.

The corresponding streaming-velocity field \mathbf{v}_2 in D1 and D2 is shown as vector and color plots in the left halves of Figs. 5(b) and 5(f). The streaming appears strikingly equal both in magnitude (66 $\mu\text{m}/\text{s}$ for D1 and 76 $\mu\text{m}/\text{s}$ for D2) and in shape and topology, but again with the center of the pattern in D1 shifted slightly away from the electrode center. The reason for this resemblance in \mathbf{v}_2 stems from the energy flux density \mathbf{S}_{ac} , which in both devices points (nearly) vertically up along the z axis above the electrodes, and is weak in between. As the (Eckart) streaming is proportional to \mathbf{S}_{ac} [51], even in microcavities [36], the streaming moves upward due to \mathbf{S}_{ac} above the electrodes and downward by recirculation between the electrodes. \mathbf{S}_{ac} has nearly the same amplitude in D1 and D2 because,

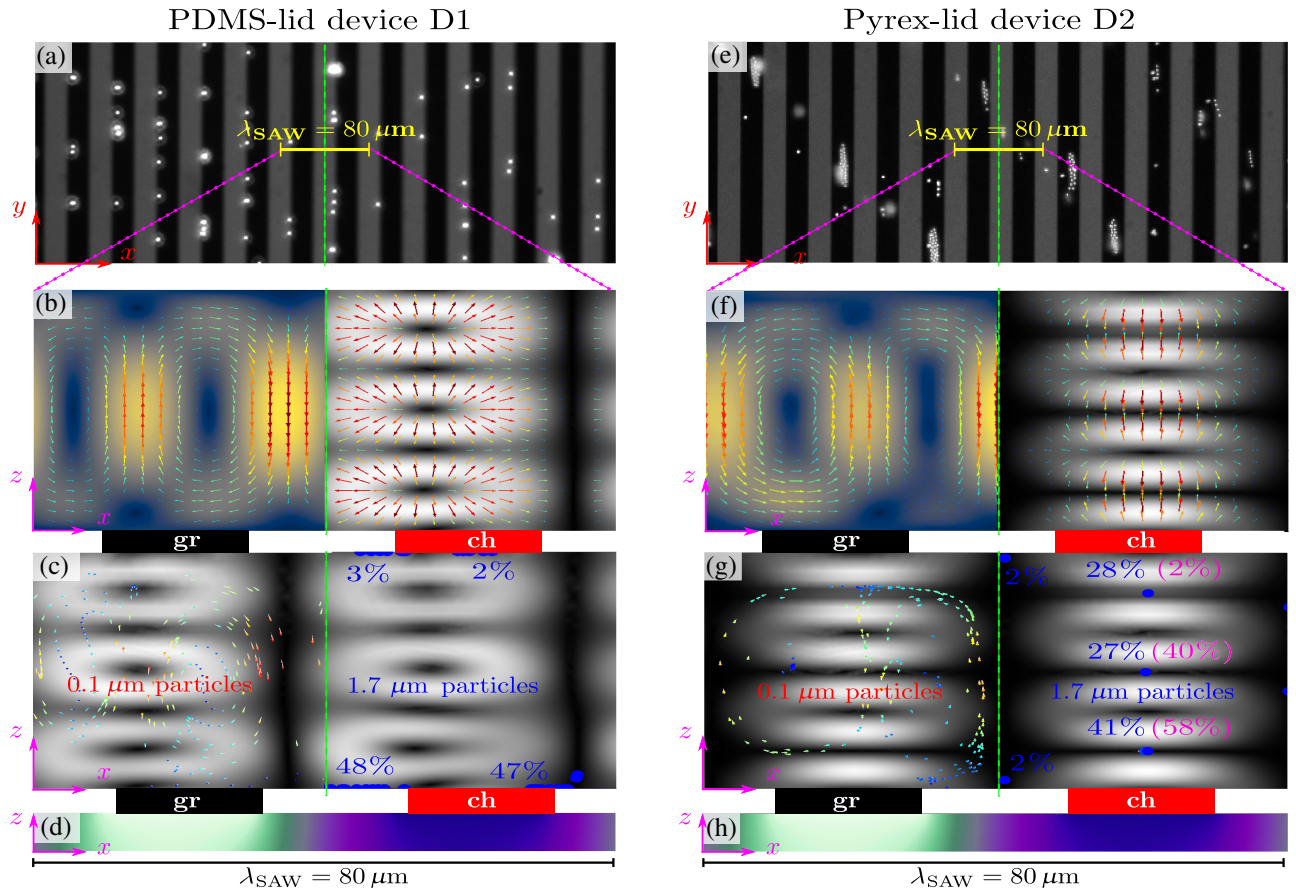


FIG. 5. Microparticle acoustophoresis in experiments and in simulations for actuation frequency $f_{\text{SAW}} = 49.9$ MHz and driving voltage $V_0 = 4.35$ V, with rescaling of the simulation from 1 to 4.35 V. (a) Top-view photograph (x - y plane) at height $z = 45$ μm above the center region of the IDT array in device D1, where suspended 1.7- μm -diameter fluorescent polystyrene particles (white) are focused above the edge of each metal electrode (black). (b) Numerical simulations in the vertical x - z plane over a single electrode pair [$6\lambda_{\text{SAW}} < x < 7\lambda_{\text{SAW}}$, the yellow line in panel (a)] in the fluid domain of device D1 with (to the left) a color plot of the magnitude $|\mathbf{v}_2|$ [from 0 (blue) to 66 $\mu\text{m/s}$ (yellow)] of the streaming velocity \mathbf{v}_2 , and (to the right) a gray-scale plot of $|\mathbf{f}^{\text{rad}}|$ [from 0 (black) to 0.4 $\text{pN}/\mu\text{m}^3$ (white)] of the acoustic radiation force density \mathbf{f}^{rad} . Superimposed are colored vector plots of \mathbf{v}_2 [from 0 (blue) to 66 $\mu\text{m/s}$ (red)] and of \mathbf{f}^{rad} [from 0 (blue) to 0.4 $\text{pN}/\mu\text{m}^3$ (red)]. (c) Color-comet-tail plot of the simulated acoustophoretic motion of 247 0.1- μm -diameter spherical polystyrene particles (to the left), superimposed on the gray-scale plot of $|\mathbf{f}^{\text{rad}}|$ from panel (b), 0.5 s after being released from initial positions on a regular 13×19 grid to the left of the green-dashed centerline. Similarly for 1.7- μm -diameter particles to the right. The comet tail indicates the direction of the velocity, with the length and color representing the speed, from 0 (dark blue) to 66 $\mu\text{m/s}$ (orange). The percentages indicate the proportion of particles accumulating in these final positions: the blue set for a homogeneous initial particle distribution, and the purple set for an inhomogeneous initial particle distribution created by 3 min of sedimentation. (d) Color plot in the vertical x - z plane below a single electrode pair $5\lambda_{\text{SAW}} < x < 6\lambda_{\text{SAW}}$ of the numerically simulated electric potential V , from -4.35 (light cyan) to 4.35 V (purple), in the lithium niobate substrate. The width and x position of the grounded and charged electrodes in the IDT pair are represented by the black (ge) and red (ce) rectangles, respectively. (e)–(h) As in (a)–(d) but for the Pyrex-lid device D2, with the image in (e) captured at height $z = 15$ μm , and in (f) the gray scale for $|\mathbf{v}_2|$ is from 0 (blue) to 76 $\mu\text{m/s}$ (yellow) and $|\mathbf{f}^{\text{rad}}|$ from 0 (black) to 7.4 $\text{pN}/\mu\text{m}^3$ (white).

although the acoustic field in D2 is much larger than in D1, it is mostly a standing wave with zero energy flux density, and the small part that is a traveling wave in D2 and that carries the energy flux density is nearly of the same magnitude as the traveling wave that constitutes the main part of the weaker acoustic field in D1.

According to Newton’s second law (13), the above-mentioned properties of the acoustic radiation force density \mathbf{f}^{rad} and streaming-velocity field \mathbf{v}_2 govern the

observable acoustophoretic motion of suspended particles. In Figs. 5(c) and 5(g), as well as in the Supplemental Material [50], the results of simulating such motion are shown for 0.1- μm - and 1.7- μm -diameter polystyrene beads in both D1 and D2, 0.5 s after starting from an initial homogeneous distribution (blue points and percentage numbers). Note that the large particles are shown only above the red “ch” electrode, but they also appear in the same pattern above the black “gr” electrode. Conversely, the small

particles are shown only above the black “gr” electrode, but they also appear in the same pattern above the red “ch” electrode. The motion of the large particles is dominated by the radiation force [52], so the different focusing of these particles seen in the right halves of Figs. 5(c) and 5(g) is explained in terms of \mathbf{f}^{rad} . Because \mathbf{f}^{rad} has no stable nodal planes in D1, all particles accumulate on the floor or the ceiling of the channel, and most of them (98%) are pushed to the regions above the electrode gaps as indicated by the vector plot in the right half of Fig. 5(c). In contrast, the stable nodal planes of \mathbf{f}^{rad} in D2, Fig. 5(g) right half, guide 96% of the particles into the three stable points above the electrode center, with 41%, 27%, and 28% at $z/H_{\text{fl}} = \frac{1}{6} = 0.17$, $\frac{3}{6} = 0.50$, and $\frac{5}{6} = 0.83$, respectively. If, instead, as in the experiments described below, we allow a sedimentation time of 3 min before turning on the acoustic field, the distribution of the focused particles changes to 58%, 40%, and 2% at $z/H_{\text{fl}} = \frac{1}{6} = 0.17$, $\frac{3}{6} = 0.50$, and $\frac{5}{6} = 0.83$, respectively.

The acoustophoretic motion of the small $0.1\text{-}\mu\text{m}$ -diameter particles is dominated by the Stokes drag from the streaming field \mathbf{v}_2 ; see the left side of Figs. 5(c) and 5(g) and the videos in the Supplemental Material [50]. The simulation shows that the particles do not settle in fixed positions but follow oblong paths in the vertical plane similar in shape to the large streaming rolls that span the entire height of the channel with an upwards motion over the electrodes and downwards in between the electrodes; see Figs. 5(b) and 5(f). In D1, \mathbf{F}^{rad} is so small that it plays essentially no role. In D2, however, \mathbf{F}^{rad} is stronger and is superposed on \mathbf{F}^{drag} to govern the acoustophoretic motion. This superposition of forces is similar to the analysis presented by Antfolk *et al.* [19], but whereas in their system the nanoparticles spiral towards a point at the center of a single flow roll, the nanoparticles above a single electrode in D2 are focused into the centerline of the two flow rolls shown in Fig. 5(f). The locations of these centerlines are defined by the vertical and horizontal nodal lines of \mathbf{f}^{rad} , represented by the black regions at the electrode gaps $x/\lambda_{\text{SAW}} = n/2$, and at the stable nodal planes $z/H_{\text{fl}} = \frac{1}{6}, \frac{5}{6}$, respectively, in the gray-scale plots in Figs. 5(f) and 5(g).

Most of these theoretical predictions are validated by experiments. After loading the particle suspension into the device, it takes about 3 min for the fluid to come to rest, during which time the $1.7\text{-}\mu\text{m}$ -diameter particles sediment slowly. This partial sedimentation shifts the homogeneous particle distribution downwards, so that the particle distribution is inhomogeneous when the acoustic field is turned on. In the experiments on the PDMS-lid device D1, the small $0.1\text{-}\mu\text{m}$ -diameter particles are observed to circulate in broad streaming rolls, and in Fig. 5(a) the large $1.7\text{-}\mu\text{m}$ -diameter particles are observed to accumulate at the floor and the ceiling in the regions near the electrode edges, mainly the left edges. In terms of the x - y in-plane streaming that is observed to flow from right to left in the

image, the left edge is downstream and the right edge is upstream. This particle behavior is partially captured by the 2D simulation in Fig. 5(c): the small particles circulate in the vertical flow rolls, while the large particles accumulate at the floor (the majority) and at the ceiling close to the edges of the electrodes, but equally distributed between the left and the right edge of any given electrode, 3% vs 2% near the ceiling, and 48% vs 47% near the floor. This left-right symmetry is broken in 3D simulations (see Sec. VI B), because the x - y in-plane streaming rolls (not included in the 2D simulation in the x - z plane) appear and push the particles towards the downstream edge of a given electrode.

In contrast to D1, in the experiments on the Pyrex-lid device D2, the large particles are seen to accumulate above the center of the electrodes near two planes, 36% of them at $z = (15 \pm 5) \mu\text{m} = (0.3 \pm 0.1)H_{\text{fl}}$ and 64% of them at $z = (30 \pm 5) \mu\text{m} = (0.6 \pm 0.1)H_{\text{fl}}$. Here, the uncertainty is estimated from the optical focal depth in the setup. These numbers are in fair agreement with the simulation results mentioned above and shown in Fig. 5(g) (purple numbers). Finally, the observed acoustophoretic focusing time of 0.1 s matches the theoretical predictions.

VI. RESULTS OF 3D MODELING

In this section, we address the more realistic but also more cumbersome simulations in three dimensions for the Pyrex-lid device D2. Even given our access to the High Performance Computing clusters at the DTU Computing Center (HPC-DTU) [53], we cannot simulate the entire chip shown in Fig. 1(a). Whereas we keep the correct dimensions for the height, we scale down the width and length to both be around 1 mm. The 3D model geometry is shown in Fig. 6, with the detailed parameter values listed in Table III. In this reduced geometry, the IDT contains only four electrode pairs and no Bragg reflectors. Although the model is downsized in two of the three dimensions, it still contains all the main components of an acoustofluidic SAW device. In the first step, the piezoelectric device, the IDT electrodes, the elastic lid, and the microchannel together with the fluid and its viscous boundary layer are combined in the calculation of the electrically induced acoustic fields. A second step, in which the acoustic radiation force and the acoustic streaming velocity are computed and used in the governing equation, predicts the acoustophoretic motion of suspended spherical particles.

A. Acoustic fields and radiation force

The 3D model shown in Fig. 6 contains 4.6 million degrees of freedom (MDOF). The calculation is distributed across 80 nodes on the HPC-DTU cluster and takes 14 h to compute. The first result is that the computed pressure and displacement fields p_1 and \mathbf{u} in three dimensions are

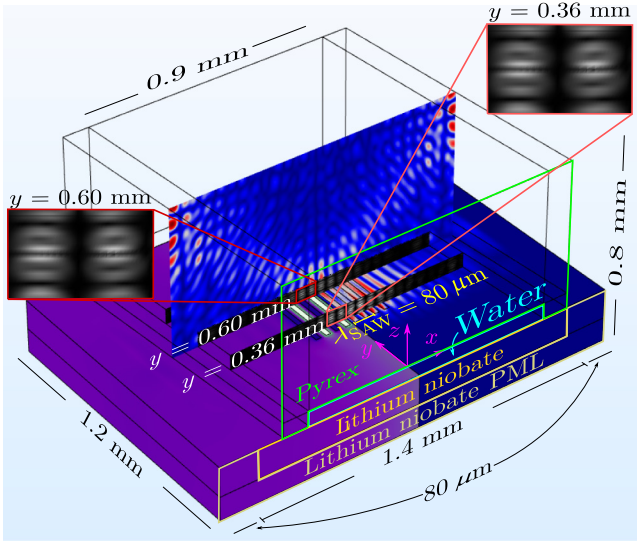


FIG. 6. 4.6 MDOF simulation of a millimeter-sized Pyrex-lid device D2 in three dimensions actuated at $f_{\text{SAW}} = 50$ MHz. Surface plot of the electric potential V [from -4.35 (purple) to 4.35 V (light cyan), rescaled from $V_0 = 1$ V] in the piezoelectric substrate, combined with a slice plot at $y = \frac{1}{2}L_{\text{sl}}$ of the acoustic-pressure magnitude $|p_1|$ [from 0 (black) to 566 kPa (yellow)] in the channel and the magnitude of the displacement $|u|$ [from 0 (blue) to 0.05 nm (red)] in the surrounding Pyrex.

both qualitatively and quantitatively similar to the ones computed in the 2D model. For vertical-slice planes parallel to the x - z plane and placed near the center of the IDT at $y = \frac{1}{2}L_{\text{sl}}$, the agreement is of course better than for those near the edge of the IDT near $y = \frac{1}{2}(L_{\text{sl}} \pm L_{\text{el}})$, but in all cases we find the period-3 structure in $|p_1|$ along the z direction seen in Fig. 4(b). Likewise, for the acoustic radiation force density, we recover the period-3 structure in $|f^{\text{rad}}|$ seen in Fig. 5(f), and the particle-focusing points in Fig. 5(g). The experimental observation of this vertical focusing thus validates this point in our 3D model.

B. Acoustic-streaming rolls

The streaming-dominated in-plane acoustophoretic motion of $0.75\text{-}\mu\text{m}$ -diameter particles suspended in the device is used in Fig. 7 to compare our model predictions with the observed particle motion. As shown in Fig. 7(a), the experimentally observed particle motion in the Pyrex-lid device D2 at the edges of the IDT electrodes is dominated by streaming rolls in the horizontal x - y plane. We compare this motion with the streaming-velocity field v_2 calculated using the 3D model, shown in Fig. 7(b). Although the model includes only a millimeter-sized sub-region of the experimental device, the same streaming pattern is evident in both the model device and the experimental device. The agreement in terms of direction,

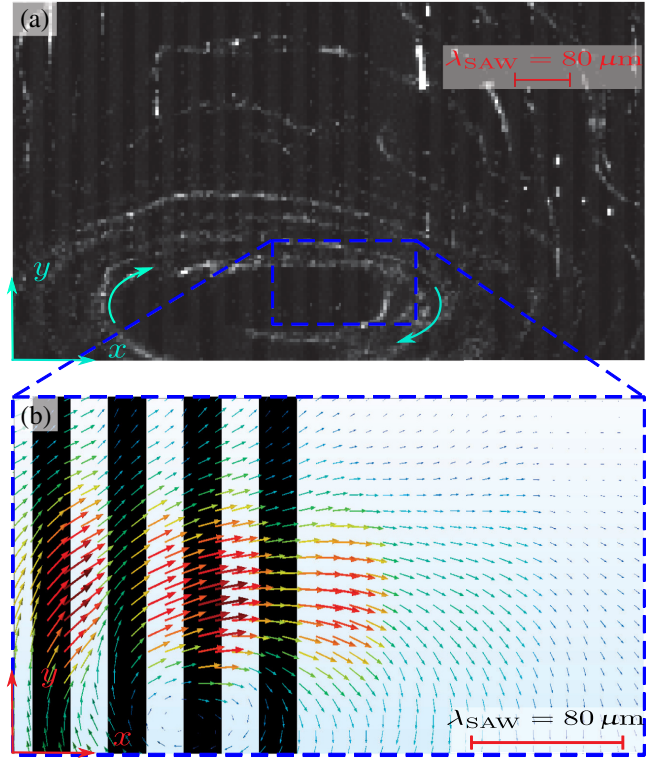


FIG. 7. Acoustic streaming in the horizontal x - y plane of the Pyrex-lid device D2. (a) Experimental top view of device D2 containing suspended $0.75\text{-}\mu\text{m}$ -diameter polystyrene particles (white), actuated at 50 MHz with $V_0 = 4.35$ V. Arrows (cyan) indicate the flow direction, and the blue dashed rectangle indicates the area shown in (b). (b) Colored-arrow plot of the simulated streaming-velocity field v_2 [from 0 (blue) to 66 $\mu\text{m/s}$ (red)] in the 3D model actuated as in panel (a). The black stripes represent the electrodes.

position, and magnitude is good, albeit with small differences. In both the simulation and the experiment, the centers of the streaming rolls are located at the edges of the electrodes, with clockwise-circulating flows. Similarly to the 2D streaming pattern in Fig. 5, the observed horizontal streaming rolls are a combination of a recirculating flow and an energy flux density, here perpendicular to and away from the IDT array. The streaming velocity in D2 near the right edge of the blue rectangular region shown in Figs. 7(a) and 7(b) is measured in the 24-electrode-pair device to be ~ 200 $\mu\text{m/s}$ and in the simulated 4-electrode-pair device to be ~ 20 $\mu\text{m/s}$, or ~ 120 $\mu\text{m/s}$ if multiplied by the ratio of the numbers of electrode pairs, $24/4$.

VII. DISCUSSION

By comparing our model simulations with measurable quantities, we find that the model can predict the overall electrical and acoustophoretic behavior of the two types of SAW devices D1 (PDMS lid) and D2 (Pyrex lid) fairly well. For the electrical response of

the device, we see good agreement between the trends near resonance of the predicted and measured values of the electrical impedance, although the predicted values are obtained in an ideal 2D model neglecting stray impedances. The predicted acoustophoretic focusing of the 1.7- μm -diameter polystyrene particles at the ceiling and floor above the edges of the electrodes in D1, and at 1/6 and 3/6 of the channel height above the center of the electrodes in D2, agrees well with experimental observations.

An interesting feature of the model is the three-half-wave resonance excited vertically in the Pyrex-lid device D2. This highlights the importance of careful consideration of the selection of materials for acoustofluidic devices, to fit the desired purpose of the device. Because a PDMS lid consists of an acoustically soft material with an acoustic impedance Z^{ac} similar to that of water ($Z^{\text{ac}}_{\text{PDMS}} = 1.19 \text{ MRayl}$, $Z^{\text{ac}}_{\text{H}_2\text{O}} = 1.49 \text{ MRayl}$), most of the energy in an acoustic wave in water impinging on the water-PDMS interface is transmitted into the PDMS, where it is dissipated as heat. Only a small fraction of the energy is reflected back into the fluid. As illustrated in Fig. 4, when the PDMS lid of the device in Ref. [23] is replaced with an acoustically hard ($Z^{\text{ac}}_{\text{Py}} = 12.47 \text{ MRayl}$) Pyrex lid, 78.6% of the wave energy is theoretically reflected back into the fluid domain from the channel lid, compared with 10.9% for a PDMS lid. The resonance buildup in the microchannel is further enhanced, as the height of the channel sustains three half-waves at the resonant frequency of the IDT, $f_{\text{res}} = c_{\text{SAW}}/\lambda_{\text{SAW}} = c_{\text{fl}}/3\lambda_{\text{wa}}$. This resonance behavior is very similar to the integer-half-wave resonances common in BAW devices, whereas the beneficial energy localization at the surface provided by the SAW is still retained. Thus, the energy loss and heat generation that occur in the piezoelectric substrate in BAW devices is mitigated in this device, whereas strong microchannel resonances can be achieved when a Pyrex lid is used in an IDT-inside SAW design. Considering this, the terms “BAW” and “SAW” seem inadequate when describing acoustofluidic devices, as the actuation scheme of the piezoelectric transducer alone does not suffice to describe the resonance behavior of the device. A more descriptive feature of a device is the nature of the wave field in the fluid, because we show the main factor determining acoustophoresis in the SAW is the difference between traveling- and standing-wave fields in the fluid.

In acoustofluidic focusing devices, a strong streaming flow is often detrimental to the desired application, as it tends to counteract the radiation force by pulling small particles away from the nodes. In the Pyrex-lid device, however, the vertical part of the streaming enhances particle focusing, as it pulls particles from areas with weak radiation force into the lower node of the acoustic radiation force, increasing the focusing efficiency.

VIII. CONCLUSION

We present a 3D model for numerical simulation of acoustophoresis by acoustic radiation forces and streaming in SAW devices taking into account the piezoelectric substrate, the IDT metal electrodes, the elastic solid defining the microchannel, the water in the microchannel, and the viscous boundary layer of the water, and implement it in the finite-element software package COMSOL Multiphysics. With such simulations, we are able to decrease the gap between the systems that we can model and those used in actual experiments. This work thus brings us closer to the point where numerical simulation can guide rational design of acoustofluidic devices.

To push acoustofluidic devices closer to medical application, the development of novel device designs beyond the proof-of-concept stage is vital. We present a close-to-scale numeric model of an acoustofluidic SAW device by expanding on previous model experiences [32,36] and the recently developed effective-boundary-layer theory [43]. With this we capture the inner workings of a nontrivial device. The model includes the linear elasticity of the defining material, the scalar pressure field of the microchannel fluid, and the piezoelectricity of the lithium niobate substrate.

Using the numeric model, we illustrate the impact that material selection in acoustofluidic chips has on acoustophoretic performance. Based on the numerically predicted acoustic fields, we propose design improvements over the previous design [23], consisting primarily of substituting the original PDMS lid with a Pyrex lid. According to our model, the new lid leads to higher energy densities and more uniform particle focusing. This causes the chip to build up strong resonances in a standing-wave field, similar to those in a BAW device. Furthermore, we use our model to predict the electrical response of a 2D model of the system, the acoustophoretic focusing of particles suspended over the IDT area of the device, and the streaming motion within devices. For each of these comparison parameters, we find agreement between predictions and experiments.

Despite our focus on a specific device design in this manuscript, the model can handle a much wider class of acoustofluidic devices. We have developed a model that can be reshaped to simulate any BAW- or SAW-device design that uses well-characterized piezoelectric transducers, Newtonian fluids, and isotropic and anisotropic linear solids.

In future work, it would be prudent to improve the model accuracy by including the temperature field to account for the thermal dependence of material parameters, particularly the bulk and dynamic viscosities of the fluid. To implement the temperature field, one must account for the various sources of heat generation in terms of mechanical losses and viscous dissipation described

in Ref. [54], which requires a good knowledge of the damping properties of each component of the device.

ACKNOWLEDGMENTS

This work is partially supported by NSF Grant No. CBET-1605574, NSF Grant No. CBET-1804963, and NIH Grant No. PSOC-1U54CA210184-01. The device fabrication is performed in part at the Cornell Nanoscale Facility (CNF), which is supported by the National Science Foundation (Grant No. ECCS-1542081).

APPENDIX: BOND AND ROTATION MATRICES

The elasticity, coupling, and permittivity properties of monocrystalline lithium niobate are listed in Ref. [38] for a Cartesian material coordinate system X, Y, Z defined as shown in Fig. 8(a). The Z axis is oriented in the growth direction, the X axis is the normal to one of the three mirror planes, and the Y axis follows from the right-hand rule, placing it within the mirror plane the X axis is normal to. The device in this manuscript, however, is manufactured on a wafer of the more commonly used 128° YX-cut lithium niobate. These are wafers of lithium niobate cut from a single crystal so that the positive surface normal forms a 128° angle with the material Y axis. In our model, we define a coordinate system x, y, z with the x axis coinciding with the material X axis, the z axis normal to the wafer surface, and the y axis determined by the right-hand rule. This global coordinate system coincides with the material coordinate system rotated by an angle $\theta = 128^\circ - 90^\circ = 38^\circ$ counterclockwise around the X axis, as shown in Fig. 8(b). In the following, we define the matrix operations necessary to determine the material parameters in the global system x, y, z from the values known in X, Y, Z .

In the usual Cartesian notation, there exists a matrix \mathbf{R} that transforms a 3×1 vector \mathbf{P}^{mt} expressed in material coordinates X, Y, Z to a vector \mathbf{P}^{gl} expressed in terms of a global coordinate system x, y, z :

$$\mathbf{P}^{\text{gl}} = \mathbf{R}\mathbf{P}^{\text{mt}}. \quad (\text{A1})$$

3×3 matrices are transformed as

$$\mathbf{e}_r^{\text{gl}} = \mathbf{R}\mathbf{e}_r^{\text{mt}}\mathbf{R}^{-1}. \quad (\text{A2})$$

For 6×1 vectors in Voigt notation, similar matrices \mathbf{M}_s , called Bond matrices, transform stress vectors $\boldsymbol{\sigma}_V^{\text{mt}}$ expressed in material coordinates into the same stress in terms of the global coordinate system $\boldsymbol{\sigma}_V^{\text{gl}}$:

$$\boldsymbol{\sigma}_V^{\text{gl}} = \mathbf{M}_\sigma \boldsymbol{\sigma}_V^{\text{mt}}. \quad (\text{A3})$$

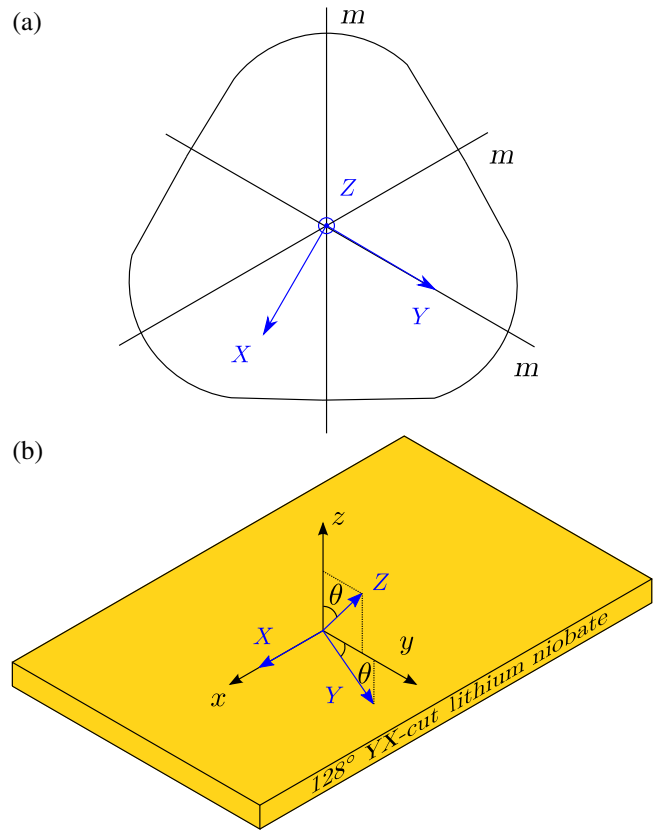


FIG. 8. (a) Top-view sketch of the material coordinate system X, Y, Z in monocrystalline hexagonal lithium niobate with three mirror planes (m). (b) 128° YX-cut lithium niobate chip showing the global coordinate system x, y, z rotated counterclockwise by $\theta = 128^\circ - 90^\circ = 38^\circ$ around the X axis relative to the material coordinate system X, Y, Z .

And, similarly to Eq. (A2), 6×6 matrices are transformed as

$$\mathbf{c}_r^{\text{gl}} = \mathbf{M}_\sigma \mathbf{c}_r^{\text{mt}} \mathbf{M}_\sigma^T. \quad (\text{A4})$$

It is important to note that Voigt-notation stress and strain vectors do not transform alike, and two transformation matrices exist in Voigt notation, i.e., $\mathbf{M}_\sigma \neq \mathbf{M}_\epsilon$. Hence, the transformation rules deviate slightly from those for 3×3 matrices.

Finally, 3×6 matrices such as the coupling tensor \mathbf{e} can be transformed using a rotation matrix and a Bond matrix:

$$\mathbf{e}_r^{\text{gl}} = \mathbf{R}\mathbf{e}_r^{\text{mt}}\mathbf{M}_\sigma^T. \quad (\text{A5})$$

Mathematically, a positive rotation by θ degrees about the material X axis is obtained from the rotation matrix $\mathbf{R}_x(\theta)$ and the Bond matrix $\mathbf{M}_{\sigma,x}(\theta)$:

$$\mathbf{R}_x(\theta) = \begin{pmatrix} 1 & 0 & 0 \\ 0 & C & S \\ 0 & -S & C \end{pmatrix}, \quad (\text{A6})$$

$$\mathbf{M}_{\sigma,x}(\theta) = \begin{pmatrix} 1 & 0 & 0 & 0 & 0 & 0 \\ 0 & \mathcal{C}^2 & \mathcal{S}^2 & 2\mathcal{C}\mathcal{S} & 0 & 0 \\ 0 & \mathcal{S}^2 & \mathcal{C}^2 & -2\mathcal{C}\mathcal{S} & 0 & 0 \\ 0 & -\mathcal{C}\mathcal{S} & \mathcal{C}\mathcal{S} & \mathcal{C}^2 - \mathcal{S}^2 & 0 & 0 \\ 0 & 0 & 0 & 0 & \mathcal{C} & \mathcal{S} \\ 0 & 0 & 0 & 0 & -\mathcal{S} & \mathcal{C} \end{pmatrix}, \quad (\text{A7})$$

using \mathcal{C} and \mathcal{S} as shorthand for $\cos(\theta)$ and $\sin(\theta)$, respectively.

-
- [1] K. Sriharan, C. Strobl, M. Schneider, A. Wixforth, and Z. Guttenberg, Acoustic mixing at low Reynold's numbers, *Appl. Phys. Lett.* **88**, 054102 (2006).
- [2] J. Shi, X. Mao, D. Ahmed, A. Colletti, and T. J. Huang, Focusing microparticles in a microfluidic channel with standing surface acoustic waves (SSAW), *Lab Chip* **8**, 221 (2008).
- [3] T. Franke, A. R. Abate, D. A. Weitz, and A. Wixforth, Surface acoustic wave (SAW) directed droplet flow in microfluidics for PDMS devices, *Lab Chip* **9**, 2625 (2009).
- [4] M. K. Tan, R. Tjeung, H. Ervin, L. Y. Yeo, and J. Friend, Double aperture focusing transducer for controlling microparticle motions in trapezoidal microchannels with surface acoustic waves, *Appl. Phys. Lett.* **95**, 134101 (2009).
- [5] J. Shi, H. Huang, Z. Stratton, Y. Huang, and T. J. Huang, Continuous particle separation in a microfluidic channel via standing surface acoustic waves (SSAW), *Lab Chip* **9**, 3354 (2009).
- [6] X. Ding, S.-C. S. Lin, B. Kiraly, H. Yue, S. Li, I.-K. Chiang, J. Shi, S. J. Benkovic, and T. J. Huang, On-chip manipulation of single microparticles, cells, and organisms using surface acoustic waves, *PNAS* **109**, 11105 (2012).
- [7] S. B. Q. Tran, P. Marmottant, and P. Thibault, Fast acoustic tweezers for the two-dimensional manipulation of individual particles in microfluidic channels, *Appl. Phys. Lett.* **101**, 114103 (2012).
- [8] J. Shi, D. Ahmed, X. Mao, S.-C. S. Lin, A. Lawit, and T. J. Huang, Acoustic tweezers: Patterning cells and microparticles using standing surface acoustic waves (SSAW), *Lab Chip* **9**, 2890 (2009).
- [9] D. J. Collins, C. Devendran, Z. Ma, J. W. Ng, A. Neild, and Y. Ai, Acoustic tweezers via sub-time-of-flight regime surface acoustic waves, *Sci. Adv.* **2**, e1600089 (2016).
- [10] A. Riaud, M. Baudoin, O. Bou Matar, L. Becerra, and J.-L. Thomas, Selective Manipulation of Microscopic Particles with Precursor Swirling Rayleigh Waves, *Phys. Rev. Appl.* **7**, 024007 (2017).
- [11] D. J. Collins, B. Morahan, J. Garcia-Bustos, C. Doerig, M. Plebanski, and A. Neild, Two-dimensional single-cell patterning with one cell per well driven by surface acoustic waves, *Nat. Commun.* **6**, 8686 (2015).
- [12] D. J. Collins, R. O'Rorke, C. Devendran, Z. Ma, J. Han, A. Neild, and Y. Ai, Self-aligned Acoustofluidic Particle Focusing and Patterning in Microfluidic Channels from Channel-based Acoustic Waveguides, *Phys. Rev. Lett.* **120**, 074502 (2018).
- [13] W. Zhou, J. Wang, K. Wang, B. Huang, L. Niu, F. Li, F. Cai, Y. Chen, X. Liu, X. Zhang, H. Cheng, L. Kang, L. Meng, and H. Zheng, Ultrasound neuro-modulation chip: Activation of sensory neurons in *Caenorhabditis elegans* by surface acoustic waves, *Lab Chip* **17**, 1725 (2017).
- [14] J. Zhang, S. Yang, C. Chen, J. H. Hartman, P.-H. Huang, L. Wang, Z. Tian, P. Zhang, D. Faulkenberry, J. N. Meyer, and T. J. Huang, Surface acoustic waves enable rotational manipulation of *Caenorhabditis elegans*, *Lab Chip* **19**, 984 (2019).
- [15] X. Ding, S.-C. S. Lin, M. I. Lapsley, S. Li, X. Guo, C. Y. Chan, I.-K. Chiang, L. Wang, J. P. McCoy, and T. J. Huang, Standing surface acoustic wave (SSAW) based multichannel cell sorting, *Lab Chip* **12**, 4228 (2012).
- [16] A. Riaud, J.-L. Thomas, E. Charron, A. Bussonnière, O. Bou Matar, and M. Baudoin, Anisotropic Swirling Surface Acoustic Waves from Inverse Filtering for On-chip Generation of Acoustic Vortices, *Phys. Rev. Appl.* **4**, 034004 (2015).
- [17] D. J. Collins, A. Neild, and Y. Ai, Highly focused high-frequency travelling surface acoustic waves (SAW) for rapid single-particle sorting, *Lab Chip* **16**, 471 (2016).
- [18] A. Liga, A. D. B. Vliegthart, W. Oosthuyzen, J. W. Dear, and M. Kersaudy-Kerhoas, Exosome isolation: A microfluidic road-map, *Lab Chip* **15**, 2388 (2015).
- [19] M. Antfolk, P. B. Muller, P. Augustsson, H. Bruus, and T. Laurell, Focusing of sub-micrometer particles and bacteria enabled by two-dimensional acoustophoresis, *Lab Chip* **14**, 2791 (2014).
- [20] Z. Mao, P. Li, M. Wu, H. Bachman, N. Mesyngier, X. Guo, S. Liu, F. Costanzo, and T. J. Huang, Enriching nanoparticles via acoustofluidics, *ACS Nano* **11**, 603 (2017).
- [21] B. Hammarström, T. Laurell, and J. Nilsson, Seed particle enabled acoustic trapping of bacteria and nanoparticles in continuous flow systems, *Lab Chip* **12**, 4296 (2012).
- [22] D. J. Collins, Z. Ma, J. Han, and Y. Ai, Continuous microvortex-based nanoparticle manipulation via focused surface acoustic waves, *Lab Chip* **17**, 91 (2017).
- [23] P. Sehgal and B. J. Kirby, Separation of 300 and 100 nm particles in Fabry-Perot acoustofluidic resonators, *Anal. Chem.* **89**, 12192 (2017).
- [24] M. Wu, Z. Mao, K. Chen, H. Bachman, Y. Chen, J. Rufo, L. Ren, P. Li, L. Wang, and T. J. Huang, Acoustic separation of nanoparticles in continuous flow, *Adv. Funct. Mater.* **27**, 1606039 (2017).
- [25] L. Johansson, J. Enlund, S. Johansson, I. Katardjiev, and V. Yantchev, Surface acoustic wave induced particle manipulation in a PDMS channel – principle concepts for continuous flow applications, *Biomed. Microdevices* **14**, 279 (2012).
- [26] F. Garofalo, T. Laurell, and H. Bruus, Performance Study of Acoustophoretic Microfluidic Silicon-Glass Devices by Characterization of Material- and Geometry-Dependent Frequency Spectra, *Phys. Rev. Appl.* **7**, 054026 (2017).
- [27] A. N. Darinskii, M. Wehnacht, and H. Schmidt, Computation of the pressure field generated by surface acoustic waves in microchannels, *Lab Chip* **16**, 2701 (2016).

- [28] M. K. Tan, J. R. Friend, O. K. Matar, and L. Y. Yeo, Capillary wave motion excited by high frequency surface acoustic waves, *Phys. Fluids* **97**, 234106 (2010).
- [29] D. Köster, Numerical simulation of acoustic streaming on surface acoustic wave-driven biochips, *SIAM J. Sci. Comput.* **29**, 2352 (2007).
- [30] H. Zhang, Z. Tang, Z. Wang, S. Pan, Z. Han, C. Sun, M. Zhang, X. Duan, and W. Pang, Acoustic Streaming and Microparticle Enrichment within a Microliter Droplet Using a Lamb-wave Resonator Array, *Phys. Rev. Appl.* **9**, 064011 (2018).
- [31] J. Lei, P. Glynne-Jones, and M. Hill, Acoustic streaming in the transducer plane in ultrasonic particle manipulation devices, *Lab Chip* **13**, 2133 (2013).
- [32] M. W. H. Ley and H. Bruus, Three-dimensional Numerical Modeling of Acoustic Trapping in Glass Capillaries, *Phys. Rev. Appl.* **8**, 024020 (2017).
- [33] N. Nama, R. Barnkob, Z. Mao, C. J. Kähler, F. Costanzo, and T. J. Huang, Numerical study of acoustophoretic motion of particles in a PDMS microchannel driven by surface acoustic waves, *Lab Chip* **15**, 2700 (2015).
- [34] J. Vanneste and O. Bühler, Streaming by leaky surface acoustic waves, *Proc. R. Soc. A* **467**, 1779 (2011).
- [35] N. R. Skov and H. Bruus, Modeling of microdevices for SAW-based acoustophoresis – A study of boundary conditions, *Micromachines* **7**, 182 (2016).
- [36] N. R. Skov, J. S. Bach, B. G. Winkelmann, and H. Bruus, 3D modeling of acoustofluidics in a liquid-filled cavity including streaming, viscous boundary layers, surrounding solids, and a piezoelectric transducer, *AIMS Math.* **4**, 99 (2019).
- [37] B. A. Auld, *Acoustic Fields and Waves in Solids* (R.E. Krieger, Malabar (FL), USA, 1990), Vol. 1.
- [38] R. Weis and T. Gaylord, Lithium niobate: Summary of physical properties and crystal structure, *Appl. Phys. A* **37**, 191 (1985).
- [39] R. H. D. Narottam, P. Bansal, and N. P. Bansal, *Handbook of Glass Properties* (Elsevier LTD, Amsterdam, NL, 1986).
- [40] E. L. Madsen, Ultrasonic shear wave properties of soft tissues and tissuelike materials, *J. Acoust. Soc. Am.* **74**, 1346 (1983).
- [41] K. Zell, J. I. Sperl, M. W. Vogel, R. Niessner, and C. Haisch, Acoustical properties of selected tissue phantom materials for ultrasound imaging, *Phys. Med. Biol.* **52**, N475 (2007).
- [42] *Material Property Database*, MIT, 77 Massachusetts Avenue, Cambridge, MA, USA, <http://www.mit.edu/6.777/matprops/pdms.htm>, accessed 21 August 2018.
- [43] J. S. Bach and H. Bruus, Theory of pressure acoustics with viscous boundary layers and streaming in curved elastic cavities, *J. Acoust. Soc. Am.* **144**, 766 (2018).
- [44] P. B. Muller and H. Bruus, Numerical study of thermo-viscous effects in ultrasound-induced acoustic streaming in microchannels, *Phys. Rev. E* **90**, 043016 (2014).
- [45] P. B. Muller and H. Bruus, Theoretical study of time-dependent, ultrasound-induced acoustic streaming in microchannels, *Phys. Rev. E* **92**, 063018 (2015).
- [46] M. Settnes and H. Bruus, Forces acting on a small particle in an acoustical field in a viscous fluid, *Phys. Rev. E* **85**, 016327 (2012).
- [47] H. Bruus, Acoustofluidics 1: Governing equations in microfluidics, *Lab Chip* **11**, 3742 (2011).
- [48] J. T. Karlsen and H. Bruus, Forces acting on a small particle in an acoustical field in a thermoviscous fluid, *Phys. Rev. E* **92**, 043010 (2015).
- [49] COMSOL Multiphysics 5.3a, <http://www.comsol.com> (2017).
- [50] The Supplemental Material at <http://link.aps.org/supplemental/10.1103/PhysRevApplied.12.044028> contains four animations of the numerically simulated acoustophoresis of 0.1- μm - and 1.7- μm -diameter particles in devices D1 and D2, corresponding to Figs. 5(c) and 5(g), respectively.
- [51] C. Eckart, Vortices and streams caused by sound waves, *Phys. Rev.* **73**, 68 (1948).
- [52] P. B. Muller, R. Barnkob, M. J. H. Jensen, and H. Bruus, A numerical study of microparticle acoustophoresis driven by acoustic radiation forces and streaming-induced drag forces, *Lab Chip* **12**, 4617 (2012).
- [53] High Performance Computing, Technical University of Denmark, <https://www.hpc.dtu.dk/> (2019).
- [54] P. Hahn and J. Dual, A numerically efficient damping model for acoustic resonances in microfluidic cavities, *Phys. Fluids* **27**, 062005 (2015).